

CrossMark
click for updatesCite this: *J. Mater. Chem. A*, 2017, 5, 4803Received 5th December 2016
Accepted 10th February 2017

DOI: 10.1039/c6ta10444d

rsc.li/materials-a

CH₃NH₂ gas induced (110) preferred cesium-containing perovskite films with reduced PbI₆ octahedron distortion and enhanced moisture stability†

Yue Chang,^{ac} Li Wang,^b Jiliang Zhang,^d Zhongmin Zhou,^a Chongwen Li,^a Bingbing Chen,^a Lioz Etgar,^e Guanglei Cui^{*a} and Shuping Pang^{*a}

We report here the discovery of a fancy interaction between cesium iodide (CsI) and methylamine (CH₃NH₂) due to the presence of the hydrogen bond. The formed CsI·xCH₃NH₂ is a liquid phase, which facilitates the large scale fabrication of highly uniform cesium-containing perovskite films with strong (110) preferred orientation by the CH₃NH₂ gas healing process. With this method, at most 10% nonpolar Cs cations could fully dope into the crystal lattice and extremely enhance the interaction of the inorganic framework with a more symmetrical PbI₆ octahedron, resulting in obvious improvement in moisture stability under continuous illumination.

1. Introduction

To look for better and cheaper alternative energy conversion materials, people have paid much attention to the development of organic–inorganic halide perovskites which are very promising for next generation solar cells.¹ Since the initiation of the use of methylammonium lead triiodide (CH₃NH₂PbI₃ or MAPbI₃) perovskites as the light harvesting layer in dye sensitized solar cells with an efficiency of 3.8%,² this field has expanded rapidly with the power conversion efficiencies (PCEs) reaching 22% at present.³ The efficiency of perovskite solar cells (PSCs) has been developed at the fastest rate among all the new generation solar devices, which is highly attributed to the optimization of the composition of perovskite and the development of film processing technologies.^{4–9} Early devices were typically fabricated from one-step spin coating deposition

followed by thermal annealing to recrystallize the perovskite layer. These films always suffer from non-uniform coverage with large amounts of voids and pinholes.¹⁰ The key reason is the formation of the rough solvent-containing intermediate phase such as a DMF–PbI₂–MAI bulk structure during the slow evaporation of the solvent.¹¹ According to the classical theory of nucleation and growth processes, the film uniformity could be improved by increasing the rate of nucleation *via* accelerating the solvent removing speed. This has been realized by the typical anti-solvent,^{12,13} hot-casting^{14,15} and vacuum-flash methods.¹⁶ The CH₃NH₂ (MA) gas healing method (MAGH) developed recently is also a very promising approach with the liquid MAPbI₃·xMA intermediate phase nucleating extremely quickly through a spontaneous degassing process even at room temperature.^{17–19} However, from the perspective of practical application, MAPbI₃ perovskite is easy to degrade when exposed to moisture.^{20–22} We have found that the (110) oriented perovskite film formed by the PbCl₂–3MAI recipe can always deliver improved air stability (Fig. S1†); several strategies have been reported to prevent perovskite from decomposing, such as Br doping to form the CH₃NH₃Pb(I_{1–x}Br_x)₃ perovskite, introducing more hydrophobic groups into the perovskite grain boundaries,^{23–25} forming a two-dimensional layered perovskite structure with introduction of long alkyl chains between the layers,^{26,27} and also cesium (Cs) metal cation doping.^{6,28} The Cs-containing perovskite layer is normally fabricated by the anti-solvent method and indeed can obviously enhance its moisture stability but without sacrificing the light absorption ability. However, the mechanism of the stability enhancement is still not deeply studied in terms of the crystal structure aspect.

Herein, we discovered the strong interaction between CsI and MA gas, which makes the MA gas healing method extremely suitable to scale up the fabrication of highly uniform Cs-containing perovskite films. The formation of the liquid CsI·xMA intermediate phase is supposed to be related to the presence of the hydrogen bond. We found that 10% Cs can fully dope into the crystal lattice forming an alloy. In the (110) oriented Cs_{0.1}–MA_{0.9}PbI₃ perovskite film, the distortion of the PbI₆ octahedron

^aQingdao Institute of Bioenergy and Bioprocess Technology, Chinese Academy of Sciences, Qingdao 266101, P. R. China. E-mail: cuigl@qibebt.ac.cn; pangsp@qibebt.ac.cn

^bQingdao University of Science and Technology, Qingdao 266042, P. R. China

^cUniversity of Chinese Academy of Sciences, Beijing 100080, China

^dDepartment of Physics and Materials Science, City University of Hong Kong, Hong Kong SAR, China

^eThe Hebrew University of Jerusalem, Institute of Chemistry, Casali Center for Applied Chemistry, Israel

† Electronic supplementary information (ESI) available. See DOI: 10.1039/c6ta10444d

is effectively reduced, characterized by reduced variation of the Pb–I bond along the *c* axis, which is considered responsible for the improvement of moisture stability.

2. Results and discussion

The interaction between CsI and MA gas is firstly studied by *in situ* optical microscopy as shown in Fig. 1A–D. One CsI crystal is placed in a transparent Petri dish (Fig. 1A). With the introduction of MA gas, the CsI crystal is gradually dissolved forming a clear liquid $\text{CsI} \cdot x\text{MA}$ around it (Fig. 1B). The distinct interface between the CsI and the formed $\text{CsI} \cdot x\text{MA}$ liquid indicates that their interaction only happens on the CsI particle surface. The MA molecules in the $\text{CsI} \cdot x\text{MA}$ liquid gradually dissolve the solid CsI together with the liquid volume continuously increasing. During this process, the MA molecules in the liquid state intermediate are constantly replenished from the outside gas state MA. That means, if such replenishment is stopped, the dissolving of CsI will also stop. Under the conditions of room temperature and atmospheric pressure, this dissolving process takes place very slowly and about 30 min is required for the full conversion (Fig. 1C). Once a fully transparent, clear drop is formed, the MA gas is removed. Then the CsI will be precipitated again in another 5 min with a totally different morphology compared with the starting CsI particle (Fig. 1D).

This CsI dissolution is related to the hydrogen bonding interaction, which inspires us to fabricate the Cs-containing perovskite films by the MA gas healing method.¹⁷ To clarify the effect of the Cs doping on the film healing process, both MAPbI_3 and $\text{Cs}_{0.1}\text{MA}_{0.9}\text{PbI}_3$ films on an FTO substrate are simultaneously studied as shown in Fig. 1E–H. These two starting films both have a grey dark colour and show no visual difference from each other (Fig. 1E). These two films suddenly fade to colourless when they are put on the top of the MA ethanol solution

(Fig. 1F). The films are kept in the colourless state for 2 seconds and then quickly removed from the MA gas environment. It is obvious that the $\text{Cs}_{0.1}\text{MA}_{0.9}\text{PbI}_3$ film darkens much faster than the film without Cs doping (Fig. 1G). Finally, both films are fully converted back to translucent reddish brown (Fig. 1H), which may be attributed to the reduction of the diffuse reflection from the film surface and the improvement of the film uniformity.

With this MA gas healing method, the $\text{Cs}_x\text{MA}_{1-x}\text{PbI}_3$ perovskite films with different Cs contents were systematically studied and their corresponding XRD patterns and UV-Vis spectra are presented in Fig. 2. All the films were fabricated from the same concentrated solution and they possessed a similar film thickness. Fig. 2A shows the XRD patterns of the samples with an Cs content of 0%, 10%, 20%, and 30%, respectively. For $x = 0$, a highly oriented perovskite film is formed, which is typical for the MA gas treated MAPbI_3 perovskite film. With the increase of x from 0 to 0.1, there is no big difference in the XRD pattern. It indicates that the 10% Cs component and the MAPbI_3 material could be simultaneously precipitated from the formed liquid intermediate and then form the pure perovskite phase. Once x is increased to 0.2, the final film is obviously phase separated with the appearance of the characteristic peaks of the yellow CsPbI_3 phase marked in Fig. 2A. It means that, with the MA gas healing method, the MAPbI_3 perovskite can only tolerate $\leq 10\%$ Cs to form a stable alloy phase. Fig. 2B is the magnified (110) peaks of all these films. It is clear that both the diffraction intensity and diffraction angle are varied along with the increase of the Cs content. The intensity firstly increases and then decreases. The strongest (110) diffraction peak of the perovskite film is obtained at $x = 0.1$, whose intensity is 2 times that of the pure MAPbI_3 film. When the Cs content increases from 10% to 30%, the (110)

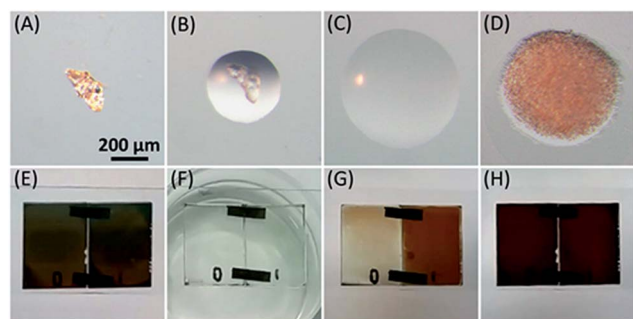


Fig. 1 (A–D) *In situ* optical microscopy observation of morphology evolution of one CsI crystal upon CH_3NH_2 gas exposure and CH_3NH_2 degassing: (A) before CH_3NH_2 gas exposure, (B) partial dissolving of the CsI crystal to liquid (15 min), (C) full conversion to liquid (30 min), and (D) CH_3NH_2 degassing and CsI back-conversion completes (35 min). (E–H) Optical photos of the MAPbI_3 (left) and $\text{Cs}_{0.1}\text{MA}_{0.9}\text{PbI}_3$ (right) films during the MA gas healing process. (E) Starting spin-coated MAPbI_3 (left) and $\text{Cs}_{0.1}\text{MA}_{0.9}\text{PbI}_3$ (right) films, (F) perovskite films in the MA gas environment (2 s), (G) perovskite films removed from the MA gas (3 s), and (H) fully recovered perovskite films with a homogenous brown colour (8 s).

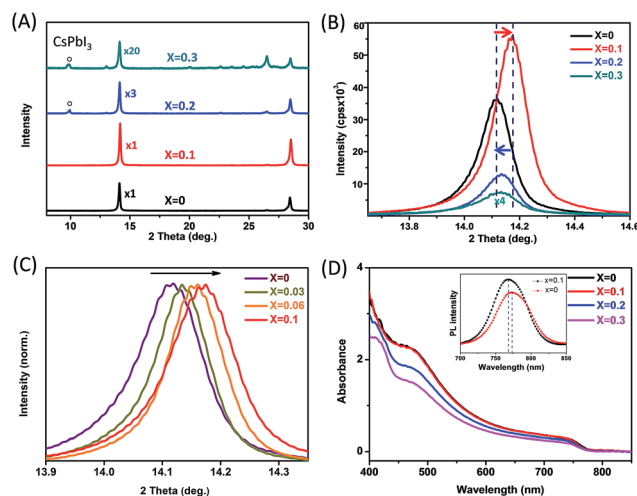


Fig. 2 XRD patterns (A–C) and UV-Vis spectra (D) of the perovskite films with different Cs contents. (A) XRD patterns of $\text{Cs}_x\text{MA}_{1-x}\text{PbI}_3$ with $x = 0, 0.1, 0.2$, and 0.3 , and their corresponding magnified (110) peaks (B). (C) Magnified (110) peak intensity of $\text{Cs}_x\text{MA}_{1-x}\text{PbI}_3$ with $x = 0, 0.03, 0.06$, and 0.1 with a normalized intensity. (D) UV-Vis absorbance spectra of $\text{Cs}_x\text{MA}_{1-x}\text{PbI}_3$ with $x = 0, 0.1, 0.2$, and 0.3 . The inset in (D) is the steady PL spectra of MAPbI_3 and $\text{Cs}_{0.1}\text{MA}_{0.9}\text{PbI}_3$.

diffraction peak intensity decreases sharply, almost only 20% remaining. Along with the variation of the diffraction intensity, the diffraction angle also changes. The measured (110) diffraction peak of pure MAPbI₃ is at 14.12°. The diffraction peak then shifts to 14.17° when 10% Cs is doped into the films. A higher content (20% and 30%) of Cs causes phase separation and the (110) diffraction peaks shift back to 14.14° and 14.13°, respectively. It is supposed that when the Cs content is increased to above 20%, most of the Cs is separated to form the CsPbI₃ phase and much less Cs remains in the mixed perovskite crystal lattice. To clearly study the alloying effect of Cs in the MAPbI₃ perovskite phase, the tiny change of $x = 0.03$ and 0.06 was further investigated as shown in Fig. 2C. There is almost a linear variation of the diffraction peaks as a function of x (0–0.1), which further indicates that the Cs content in the range of 0–10% can efficiently dope the MAPbI₃ crystal lattice. This doping behavior is also evidenced by the UV-Vis spectra in Fig. 2D. The Cs doping with $x = 0.1$ causes no obvious decrease of the absorption intensity but only a minimal blue shift of the absorption onset than the pure MAPbI₃, with the bandgap increasing from 1.586 eV to 1.602 eV as shown in Fig. S2,† which is also consistent with the steady state Photo Luminescence (PL) spectra shown in the inset in Fig. 2D. With x further increased from 0.1 to 0.3, the absorption intensity is highly reduced because of the formation of the light colored CsPbI₃ phase in the film.

The scanning electron microscopy (SEM) images in Fig. 3A–D show the top-surface morphologies of the MA gas treated Cs_xMA_{1-x}PbI₃ films. The MAPbI₃ film treated with MA gas has full coverage morphology with a very low roughness (Fig. 3A). After 10% Cs is doped into the film, a more compact film is obtained as shown in Fig. 3B. The sequential elemental distribution mapping of the Cs_{0.1}MA_{0.9}PbI₃ film in Fig. S3† confirms that Cs is homogeneously distributed on the entire film. Once

the Cs content is increased to 20% (Fig. 3C) and 30% (Fig. 3D), a rod-like structure is formed and embedded in the perovskite films. The rod-like structure should be the orthorhombic phase CsPbI₃. Between the rod-like CsPbI₃ structures, the grain size of the matrix Cs_xMA_{1-x}PbI₃ is reduced to about 100 nm, which may be associated with the growth restriction from the surrounding CsPbI₃ crystals. Fig. 3E and F are the cross-sectional image of the MAPbI₃ and Cs_{0.1}MA_{0.9}PbI₃ perovskite films on a mesoporous TiO₂ layer. The thickness of the perovskite layers is about 600 nm. With respect to the MAPbI₃ film, the mesoporous layer is filled more compactly for the Cs_{0.1}MA_{0.9}PbI₃ perovskite film, which is considered to be extremely important for the photovoltaic devices.

The film morphology and photo-absorption properties strongly depend on the gas treating time as evidenced in the SEM (Fig. S4†) and UV-Vis spectra (Fig. S5†), respectively. MA gas treating for 2 s is enough for the film sample to fully transform into a liquid phase with a balance of viscosity and wettability for film processing. The performance of PSCs against different MA gas treatment periods and thermal annealing times is also systematically explored as shown in Fig. S6 and S7.† Based on these optimizations, the photovoltaic devices upon incorporation of different amounts of Cs are assembled and studied. Their J - V curves with the reverse (from open-circuit voltage V_{oc} to short-circuit current J_{sc}) scanning direction are shown in Fig. 4A, with the external quantum efficiency (EQE)

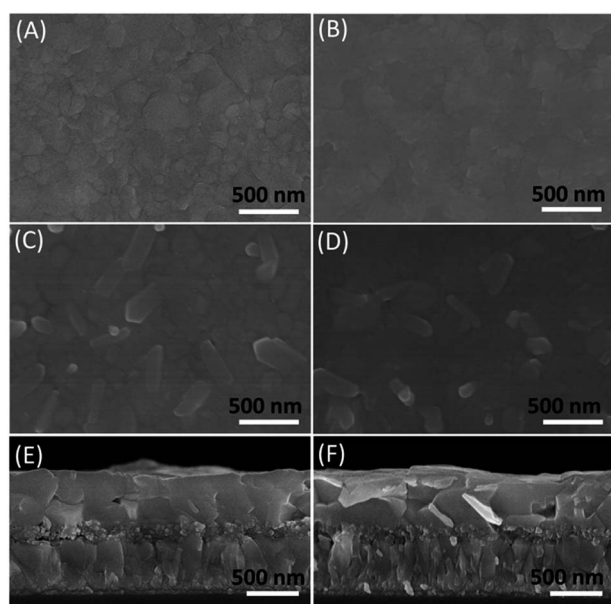


Fig. 3 (A–D) SEM images of Cs_xMA_{1-x}PbI₃ with $x = 0, 0.1, 0.2$, and 0.3 , and the cross-section image of MAPbI₃ (E) and Cs_{0.1}MA_{0.9}PbI₃ (F).

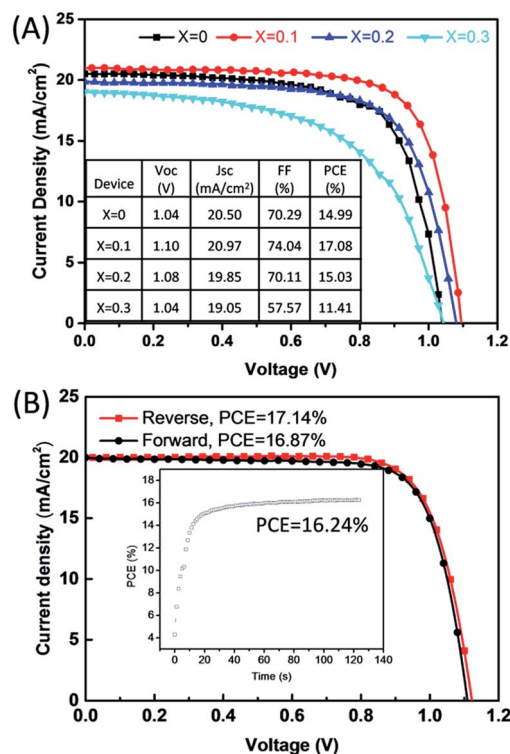


Fig. 4 (A) J - V characteristics of the Cs_xMA_{1-x}PbI₃ PSCs with different Cs contents with the detailed parameter table of PSCs shown in the inset. (B) J - V characteristics of the champion Cs_{0.1}MA_{0.9}PbI₃ perovskite device for forward and reverse scans. The inset in (B) is the stabilized PCE at the maximum power point.

measurement for MAPbI₃ and Cs_{0.1}MA_{0.9}PbI₃ in Fig. S8.† Their corresponding parameters are summarized in the inset table. The MAPbI₃ solar cell presents an efficiency of 14.99%, with V_{oc} of 1.04 V, J_{sc} of 20.50 mA cm⁻², and FF of 70.29%. With the increase of Cs content in the perovskite film, the efficiency is firstly enhanced and then decreased. 10% Cs doping delivers the highest efficiency of 17.08% with V_{oc} of 1.10 V, J_{sc} of 20.97 mA cm⁻², and FF of 74.04%. With respect to the pure MAPbI₃ device, all the device parameters are improved. The improvement is attributed to the reduced recombination rate of the photo-induced carriers in the Cs_{0.1}MA_{0.9}PbI₃ perovskite film as evidenced by the time-resolved PL and the open circle voltage decay (OCVD) measurements in Fig. S9 and S10.† Further increasing the Cs content in the film causes the phase separation and thus highly degrades the device performance. For the champion Cs_{0.1}MA_{0.9}PbI₃ perovskite device, forward and reverse scan results are presented in Fig. 4B. The reverse scan efficiency is 17.14% with less hysteresis. The PCE output at the maximum power point (inset in Fig. 4B) indicates that the light soaking is still required for the Cs doped perovskite solar cells and a stable PCE of 16.24% is already reached.

Since the MA gas healed perovskite film has strong (110) preferred orientation as illustrated in Fig. 5A, we further studied the evolution of the crystal structure after 10% Cs doping, by employing Rietveld refinements (Fig. 5B) based on their X-ray powder diffraction patterns (Fig. S11†). The phase-pure MAPbI₃ and the Cs_{0.1}MA_{0.9}PbI₃ perovskite (space group *I4cm*) are obtained and the Pb–I bond lengths are obviously changed along

the *c* axis (Fig. 5B). The instability of MAPbI₃ perovskite is characterized by the formation of PbI₂, instead of other MAPbI₃ polymorphs containing a generally distorted PbI₆ octahedron, implying that the stability is mainly related to the local structure PbI₆ octahedron. In ABX₃ perovskite, actually, the influence of the distorted BX₆ octahedron on the structural stability and electronic properties has been studied extensively.²⁹ In the refined structure of MAPbI₃ perovskite here, the Pb–I1, Pb–I1' and Pb–I2 bonds are 3.12(2) Å, 3.21(2) Å and 3.17(1) Å, respectively, very close to the reported values given by single-crystal samples.³⁰ The large difference of the Pb–I bond distance along the *c* axis makes the PbI₆ octahedron highly distorted and it is surprising that the stability of its thin film can be improved if the penetration of water along the *c* axis was suppressed. For example, the (110) oriented perovskite film is more stable than its bulk form. It is also noted that I1 and I1' take an equivalent position crystallographically. Inequivalent Pb–I1 and Pb–I1' bonds are likely due to the polarity of MA molecules which also align along the *c* axis. Thus the substitution of polar MA by nonpolar Cs will reduce the distortion along the *c* axis. In Cs_{0.1}MA_{0.9}PbI₃, as expected, the Pb–I bond lengths highly evolve with the Pb–I1, Pb–I1' and Pb–I2 bonds which are 3.14(2) Å, 3.19(2) Å and 3.17(1) Å, respectively. The distortion angle of the PbI₆ octahedron in MAPbI₃ is 87.3(2)°, while the distortion angle of the PbI₆ octahedron in Cs_{0.1}MA_{0.9}PbI₃ is 87.6(2)°. This means that the symmetry of the lattice has been slightly improved due to the doping of 10% Cs into the perovskite structure. The Pb–I1' bond distance is reduced from 3.21 Å to 3.19 Å, while the Pb–I1 bond distance is elongated from 3.12 Å to 3.14 Å, which is also extremely promising for the improvement of the stability.

To quickly check the improvement of the moisture stability after Cs doping, the decomposition process is accelerated by putting the unprotected MAPbI₃ and Cs_{0.1}MA_{0.9}PbI₃ films directly under one sun illumination (AM 1.5) with the light intensity of 100 mW cm⁻² at a relative humidity of 40%. It is obvious that, after 3 h continuous light soaking, the pure MAPbI₃ film obviously decomposes with the PbI₂ diffraction peaks at 12.5° as shown in Fig. 5C, while there are no obvious PbI₂ peaks in the Cs doped perovskite film shown in Fig. 5D under the same conditions. The SEM images after illumination are displayed in Fig. 5(E) and (F). The MAPbI₃ perovskite film shows obvious decomposition after the continuous light exposure. In contrast, the morphology stability of the Cs doped sample is greatly improved as evidenced in Fig. 5F. Compared to the pure perovskite film, the improvement of stability for the Cs doped perovskite film is also proved by the UV-Vis absorbance spectra in Fig. S12.† Similarly, the stability of the two types of PSC devices with Spiro-OMeTAD as the hole transport material and silver as the cathode was also compared. As expected, the Cs_{0.1}MA_{0.9}PbI₃ solar cell is more stable than the MAPbI₃ solar cell (Fig. S13†).

3. Conclusions

In summary, we have demonstrated the interaction between CsI and MA. The formed CsI·*x*MA is a liquid phase. Benefiting

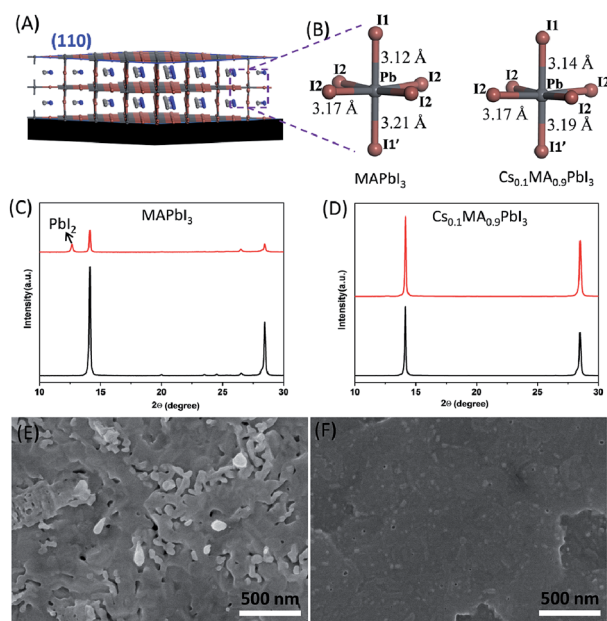


Fig. 5 (A) Schematic illustration of the (110) preferred perovskite film. (B) PbI₆ unit of MAPbI₃ and Cs_{0.1}MA_{0.9}PbI₃ perovskites, respectively. The comparison of the XRD patterns of (C) MAPbI₃ and (D) Cs_{0.1}MA_{0.9}PbI₃ perovskite films before and after continuous illumination (AM 1.5) for 3 h without any protection in air with a humidity of 40%. (E and G) The corresponding SEM images of the MAPbI₃ (E) and Cs_{0.1}MA_{0.9}PbI₃ (F) perovskite films after continuous one sun illumination for 3 h.

from this phenomenon, the (110) oriented Cs-containing perovskite films are fabricated by the MA gas healing method. It is found that, based on this method, 10% Cs could dope into the crystal lattice and the efficiency is improved from 15% to 17%. Most importantly, the device based on $\text{Cs}_{0.1}\text{MA}_{0.9}\text{PbI}_3$ is much more stable than that based on MAPbI_3 under continuous illumination when kept unsealed under ambient conditions. The reason is attributed to the formation of a more compact perovskite film and reduced PbI_6 octahedron distortion, where variation of Pb–I bonds is suppressed along the *c* axis after the nonpolar Cs doping. This study implies that the symmetrical characteristic of the inorganic framework and the film orientation are both very important for the enhancement of the moisture stability.

4. Experimental section

MAI and TiO_2 gels were all synthesized in the lab as we reported previously.¹⁷ CsI was purchased from Sigma-Aldrich. The $\text{MA}_{1-x}\text{CS}_x\text{PbI}_3$ precursor solutions (50 wt%) were prepared by dissolving PbI_2 , MAI and CsI (1 : 1 – *x* : *x* by molar) in *N,N*-dimethylformamide (DMF; 99.8%). The solutions were pre-heated and stirred at 60 °C for 1 h before use. A 30 nm thick dense TiO_2 layer and a 200 nm thick TiO_2 porous layer were deposited on FTO glass by spin coating, followed by heating at 550 °C for 30 min in air. The $\text{MA}_{1-x}\text{CS}_x\text{PbI}_3$ precursor solutions prepared as described above were subsequently spin coated on the FTO/ TiO_2 substrates at 4000 rpm for 30 s, followed by annealing at 100 °C for different times as discussed in the ESI.† Then the $\text{MA}_{1-x}\text{CS}_x\text{PbI}_3$ perovskite layer was healed using the MIDH method before depositing the HTM and the Ag layers. That is the perovskite film was exposed to MA gas for a few seconds at room temperature and then removed to an ambient atmosphere rapidly. The HTM prepared as described in the previous literature¹⁷ was deposited on the top of the healed perovskite film by spin-coating the spiro-MeOTAD solution at 3000 rpm for 30 s. Finally, a 100 nm Ag electrode was thermally evaporated to complete the PSC assembly.

XRD spectra were measured by using a Bruker-AXS Micro diffractometer (D8 ADVANCE) with Cu K α radiation (1.5406 Å). The optical absorbance spectra were measured by using a UV-Vis/NIR spectrophotometer (U-4100, Hitachi). Top view and cross-section SEM images and energy disperse spectra (EDS) were obtained with a field-emission scanning electron microscope (S-4800, Hitachi). *I*–*V* curves of the as-fabricated PSCs with different scanning directions were measured using a 2400 Sourcemeter (Keithley, USA) under simulated one-sun AM 1.5G 100 mW cm^{–2} intensity (Oriol Sol3A Class AAA, Newport, USA). The maximum-power output stability of the PSCs was measured by monitoring the *J* output at the maximum-power *V* bias. The typical active area of PSCs is 0.09 cm² defined by a metal mask. The intensity of the one-sun AM 1.5G illumination was calibrated using a Si-reference cell certified by the National Renewable Energy Laboratory. The OCVD measurements were gained by using an electrochemical workstation (Bio-Logic science instruments). And External quantum efficiency (EQE)

measurements were carried out on an EQE measurement setup (Newport, USA).

Acknowledgements

This work was financially supported by the International S&T Cooperation Program of China (2015DFG62670), the National Natural Science Foundation (51672290, 21671196, and 61604156), the Youth Innovation Promotion Association of CAS (2015167), and the Qingdao Key Lab of solar energy utilization and energy storage technology.

References

- 1 A. Polman, M. Knight, E. C. Garnett, B. Ehrler and W. C. Sinke, *Science*, 2016, **352**, 4424.
- 2 A. Kojima, K. Teshima, Y. Shirai and T. Miyasaka, *J. Am. Chem. Soc.*, 2009, **131**, 6050.
- 3 [https://en.wikipedia.org/wiki/Solar_cell#/media/File:PVeff_\(rev160812\).jpg](https://en.wikipedia.org/wiki/Solar_cell#/media/File:PVeff_(rev160812).jpg), 2016.
- 4 D. P. McMeekin, G. Sadoughi, W. Rehman, G. E. Eperon, M. Saliba, M. T. Hörlantner, A. Haghighirad, N. Sakai, L. Korte, B. Rech, M. B. Johnston, L. M. Herz and H. J. Snaith, *Science*, 2016, **351**, 151.
- 5 N. J. Jeon, J. H. Noh, W. S. Yang, Y. C. Kim, S. Ryu, J. Seo and S. I. Seok, *Nature*, 2015, **517**, 476.
- 6 J.-W. Lee, D.-H. Kim, H.-S. Kim, S.-W. Seo, S. M. Cho and N.-G. Park, *Adv. Energy Mater.*, 2015, **5**, 1501310.
- 7 M. Saliba, T. Matsui, K. Domanski, J.-Y. Seo, A. Ummadisingu, S. M. Zakeeruddin, J.-P. Correa-Baena, W. R. Tress, A. Abate, A. Hagfeldt and M. Grätzel, *Science*, 2016, **354**, 206.
- 8 Q. Chen, H. Zhou, Z. Hong, S. Luo, H. S. Duan, H. H. Wang, Y. Liu, G. Li and Y. Yang, *J. Am. Chem. Soc.*, 2014, **136**, 622.
- 9 Z. Xiao, C. Bi, Y. Shao, Q. Dong, Q. Wang, Y. Yuan, C. Wang, Y. Gao and J. Huang, *Energy Environ. Sci.*, 2014, **7**, 2619.
- 10 Y. Zhao and K. Zhu, *J. Phys. Chem. C*, 2014, **118**, 9412.
- 11 Y. Zhou, O. S. Game, S. Pang and N. P. Padture, *J. Phys. Chem. Lett.*, 2015, **6**, 4827.
- 12 N. J. Jeon, J. H. Noh, Y. C. Kim, W. S. Yang, S. Ryu and S. I. Seok, *Nat. Mater.*, 2014, **13**, 897.
- 13 M. Xiao, F. Huang, W. Huang, Y. Dkhissi, Y. Zhu, J. Etheridge, A. Gray-Weale, U. Bach, Y.-B. Cheng and L. Spiccia, *Angew. Chem., Int. Ed.*, 2014, **53**, 9898.
- 14 W. Nie, H. Tsai, R. Asadpour, J.-C. Blancon, A. J. Neukirch, G. Gupta, J. J. Crochet, M. Chhowalla, S. Tretiak, M. A. Alam, H.-L. Wang and A. D. Mohite, *Science*, 2015, **347**, 522.
- 15 Y. C. Zheng, S. Yang, X. Chen, Y. Chen, Y. Hou and H. G. Yang, *Chem. Mater.*, 2015, **27**, 5116.
- 16 X. Li, D. Bi, C. Yi, J.-D. Décoppet, J. Luo, S. M. Zakeeruddin, A. Hagfeldt and M. Grätzel, *Science*, 2016, **353**, 58.
- 17 Z. Zhou, Z. Wang, Y. Zhou, S. Pang, D. Wang, H. Xu, Z. Liu, N. P. Padture and G. Cui, *Angew. Chem., Int. Ed.*, 2015, **54**, 9705.

- 18 S. Pang, Y. Zhou, Z. Wang, M. Yang, A. R. Krause, Z. Zhou, K. Zhu, N. P. Padture and G. Cui, *J. Am. Chem. Soc.*, 2016, **138**, 750.
- 19 Y. Zhou, M. Yang, S. Pang, K. Zhu and N. P. Padture, *J. Am. Chem. Soc.*, 2016, **138**, 5535.
- 20 J. Yang, B. D. Siempelkamp, D. Liu and T. L. Kelly, *ACS Nano*, 2015, **9**, 1955.
- 21 A. M. A. Leguy, Y. Hu, M. Campoy-Quiles, M. I. Alonso, O. J. Weber, P. Azarhoosh, M. van Schilfgaarde, M. T. Weller, T. Bein, J. Nelson, P. Docampo and P. R. F. Barnes, *Chem. Mater.*, 2015, **27**, 3397.
- 22 J. A. Christians, P. A. Miranda Herrera and P. V. Kamat, *J. Am. Chem. Soc.*, 2015, **137**, 1530.
- 23 X. Li, M. Ibrahim Dar, C. Yi, J. Luo, M. Tschumi, S. M. Zakeeruddin, M. K. Nazeeruddin, H. Han and M. Grätzel, *Nat. Chem.*, 2015, **7**, 703.
- 24 Y. Zhao, J. Wei, H. Li, Y. Yan, W. Zhou, D. Yu and Q. Zhao, *Nat. Commun.*, 2016, **7**, 10228.
- 25 S. Yang, Y. Wang, P. Liu, Y.-B. Cheng, H. J. Zhao and H. G. Yang, *Nat. Energy*, 2016, **1**, 15016.
- 26 H. Tsai, W. Nie, J.-C. Blancon, C. C. Stoumpos, R. Asadpour, B. Harutyunyan, A. J. Neukirch, R. Verduzco, J. J. Crochet, S. Tretiak, L. Pedesseau, J. Even, M. A. Alam, G. Gupta, J. Lou, P. M. Ajayan, M. J. Bedzyk, M. G. Kanatzidis and A. D. Mohite, *Nature*, 2016, **536**, 312.
- 27 I. C. Smith, E. T. Hoke, D. Solis-Ibarra, M. D. McGehee and H. I. Karunadasa, *Angew. Chem., Int. Ed.*, 2014, **53**, 11232.
- 28 C. Yi, J. Luo, S. Meloni, A. Boziki, N. Ashari-Astani, C. Grätzel, S. M. Zakeeruddin, U. Röthlisberger and M. Grätzel, *Energy Environ. Sci.*, 2016, **9**, 656.
- 29 Z. Wang, Z. Shi, T. Li, Y. Chen and W. Huang, *Angew. Chem., Int. Ed.*, 2016, **55**, 2.
- 30 C. C. Stoumpos, C. D. Malliakas and M. G. Kanatzidis, *Inorg. Chem.*, 2013, **52**, 9019.